Available online at www.sciencedirect.com

jmr&t Journal of Materials Research and Technology

journal homepage: www.elsevier.com/locate/jmrt

Original Article

Neutron Bragg edge imaging for strain characterization in powder bed additive manufacturing environments

Shieren Sumarli [a,b], *Efthymios Polatidis* [a], *Florencia Malamud* [a,d], *Matteo Busi* [a], *Claire Navarre* [c], *Reza Esmaeilzadeh* [c], *Roland Logé* [c], *Markus Strobl* [a,*]

[a] *Paul Scherrer Institute, Laboratory of Neutron Scattering and Imaging, Forschungsstrasse 111, 5232, Villigen, Switzerland*

[b] *École Polytechnique Fédérale de Lausanne, EDMX-Materials Science and Engineering, 1015 Lausanne, Route Cantonale, Switzerland*

[c] *Thermomechanical Metallurgy Laboratory - PX Group Chair, Ecole Polytechnique Fédérale de Lausanne (EPFL), CH-2002, Neuchâtel, Switzerland*

[d] *Laboratorio Argentino de Haces de Neutrones (LAHN), Comisión Nacional de Energía Atómica y CONICET, Avenida Bustillo 9500, San Carlos de Bariloche, Rio Negro, 8400, Argentina*

ARTICLE INFO

Article history:
Received 29 August 2022
Accepted 7 November 2022
Available online 11 November 2022

Keywords:
Laser powder bed fusion
Neutron bragg edge imaging
Neutron transmission analysis
Neutron diffraction
Non-destructive strain measurement
Strain mapping

ABSTRACT

Spatially resolved studies of crystalline structures, e.g. lattice spacings, are enabled by recording the transmitted spectra in neutron Bragg edge imaging. The recorded signals are, however, a result of through-thickness averaging of the probed specimen in the beam direction. Therefore, it is challenging to extract the strain distribution when the strain varies across the thickness, which applies for studies on different materials or material states along the beam. Here we introduce the approach to disentangle contributions to the recorded signals, i.e. separating the transmission spectra of two different material states. This is particularly applicable to powder bed additive manufacturing environments where operando strain characterization of the printed specimen using neutrons is intended. In this work, Laser Powder Bed Fusion (PBF-LB/M)-built 316L and IN718 samples embedded in their corresponding powders are used, extracting the desired spectra of the printed specimen. The disentanglement is proven to be satisfactory by obtaining coinciding strain maps of identical specimens embedded in powder layers of different thicknesses. Furthermore, the obtained residual strain distributions of 316L samples were verified by conventional neutron diffraction with lower spatial resolution due to the gauge volume averaging.

* Corresponding author.
E-mail address: markus.strobl@psi.ch (M. Strobl).

https://doi.org/10.1016/j.jmrt.2022.11.047

1. Introduction

Neutron Bragg edge imaging (BEI) [1] has proven to be an efficient tool for the nondestructive characterization of internal structures of polycrystalline materials extending image analyses to the domain of crystal lattice spacings, targeting e.g. strain fields [2–5], textures [6,7] and phase distributions [8–11]. One of the main differences between neutron Bragg edge imaging and its reciprocal space equivalent, neutron diffraction, is the recorded signals. While neutron diffraction focuses on detecting scattered radiation deviating from the incident beam, neutron Bragg edge imaging is concerned with the transmitted beam intensity.

Neutron diffraction is an established and powerful method to quantitatively assess strains within well-defined gauge volumes deep in the bulk of metallic materials and components. The gauge volume of a specific measurement is defined by the collimation of the incoming and diffracted beam, which is typically probed in a 90° geometry, resulting in a cubic or parallelepiped gauge volume. Information about multiple lattice plane families can be obtained at a fixed scattering angle of 90° by using pulsed polychromatic beams. The obtained information is averaged over the determined gauge volume which is typically in the order of cubic millimeters. With a symmetric detector arrangement of ± 90°, which is standard for the polychromatic time-of-flight (ToF) diffractometers exploiting the wavelength resolution of a pulsed neutron beam, two principal strain directions are probed simultaneously. To measure additional components, the sample has to be rotated correspondingly. By doing so, neutron diffraction is suitable for characterizing the full stress tensor. Moreover, to perform spatially resolved strain measurements in cubic-centimeter-sized samples, it is necessary to step-wise scan with the gauge volume through the sample. When steep strain gradients exist, due to the averaging effect within the gauge volume, the method fails to capture them precisely.

Compared to the well-established neutron diffraction, neutron Bragg edge imaging offers the possibility of deriving two-dimensional strain maps through single-exposure full-field measurements with superior spatial resolution [2,4,12]. The approach is limited to the strain direction along the beam, two-dimensional resolution and averaging over the thickness along the beam. However, current developments are pursued to extend studies to 3D strain tomography [13–16]. On the other hand, time-resolved studies can also be considered, like realized e.g. for the evolution of phase transitions [17]. The enhanced spatial resolution of Bragg edge imaging provides the opportunity e.g. for studies of variations of strains (inhomogeneities) that might remain undetected otherwise, and can also provide guidance for more detailed local investigations, e.g. through diffraction. While neutron Bragg edge imaging and neutron diffraction feature different strengths and weaknesses, they can often be used as complementary tools. Several studies of residual stress applied both methods, particularly when through-thickness strain averaging is allowed. Such an approach can be of substantial value for example in the field of development and optimization of manufacturing processes [2,18–21].

Due to the fact that two-dimensional Bragg edge imaging is averaging strains in the beam direction, mapping strain fields where the strain varies along the beam path remains a challenging task. This also applies when Bragg edges of different materials, e.g. in additively manufactured multi-materials, or different material states, e.g. solid and powder, overlap. When intending, for example, to map strains in additively manufactured material during the production process, it has to be considered that the sample is surrounded by powder of the same alloy as the built sample. Here we introduce an approach to disentangle the signal from powder and manufactured specimen in a geometry resembling in-situ strain mapping during powder bed additive manufacturing in order to reveal the strains in the specimen. The results of Bragg edge strain mapping are then compared with and verified by diffraction measurements of the same sample systems.

2. Materials and methods

2.1. Sample preparation

Austenitic stainless steel 316L and Ni-based superalloy Inconel 718 (IN718) were selected for this study. The samples were additively manufactured using Laser Powder Bed Fusion (PBF-LB/M) on a TRUMPF TruPrint 1000 machine equipped with a fiber laser operated in continuous wave (CW) mode. The machine has a maximum power of 200 W, a wavelength of 1070 nm and is generating a focused beam with a Gaussian intensity distribution implying a spot diameter at the focal plane $(1/e^2)$ of 30 μm. The laser was focused at the working plane supported by a stainless steel 316L base plate with a diameter of 99 mm. The powder used was provided by Oerlikon Metco, Switzerland with a particle size of 15–45 μm. A powder layer thickness of 20 μm was used to build the samples without a specific support structure. Processing was under Ar atmosphere and the O_2 content was kept below 0.02%. A bidirectional scanning strategy with a 67° rotation per layer was applied to minimize texture in the transverse directions [22].

The built sample geometry is described by a 12 × 8 mm^2 cross-section with different building heights. A total of four 316L samples and three IN718 samples were produced with processing parameters, i.e. laser power, scanning speed and hatching distance, as listed in Table 1. The processing parameters were chosen to either intentionally introduce lack of fusion (LoF) pores in the bulk as a result of insufficient energy

Table 1 – List of the sample labels and their respective combination of dimension, PBF-LB/M processing parameters and the intended processing regime.

Sample label	A	B	C	D	E	F	G
Material			316L			IN718	
Processing regime	CM	CM	LoF	LoF	CM	LoF	LoF
Laser power (W)	80	80	50	50	90	85	85
Scanning speed (mm/s)	800	800	800	800	880	1450	1450
Layer thickness (μm)	20	20	20	20	20	20	20
Building height (mm)	15	30	30	30	30	30	30
ID of Al tube (mm)	17.75	17.75	17.75	22.7	17.75	17.75	22.7

input to completely melt the powder, or to produce dense samples within the conduction mode (CM) processing regime which is suited to produce the highest density. Fig. 1 exemplarily shows the micrographs of samples produced in LoF and conduction mode regimes. In order to mimic the condition during PBF-LB/M processing, the samples are surrounded by their corresponding powder and enclosed by an aluminum tube. Two different inner diameters (ID) of the Al tube were selected to enclose the samples with powders of different amounts and hence different projected thickness distributions.

2.2. Instrumentation

The experiments were performed at the Pulse-OverLap-DIffractometer (POLDI) [23] at the Swiss spallation neutron source (SINQ) of the Paul Scherrer Institute (PSI), Switzerland. POLDI is equipped with a 350 mm-radius chopper system with 32 slits partitioned in four identical sequences of eight pseudorandomly distributed slits. Each slit has a height of 40 mm, corresponding to the beam height, and a width of 4 mm, equivalent to an angular width of 0.65° yielding a duty cycle of 5.8%. The multi-slit chopper at the continuous neutron source allows multiple frame overlap, i.e. neutrons of several different pulses, related to different chopper slits, may reach the detector at once. The system is used to enhance the efficiency, which is directly proportional to the chopper duty cycle, up to 1.5 orders of magnitude when compared to a conventional ToF diffractometer, without frame overlap, while not sacrificing resolution and wavelength bandwidth, suitable for structural analysis applications.

POLDI features one diffraction detector bank at a 90° angle to the incoming beam direction as illustrated in Fig. 2(a). The probed lattice strain direction is, therefore, inclined at 45° with respect to the incoming and diffracted beam. With a scattering angle 2θ of around 90°, a rectangular gauge volume is formed by the opening of the slits, which determine the incident beam shape and size, as well as the radial collimator in front of the diffraction detector that defines the third dimension of the volume. Currently, three different radial collimators with resolutions of 0.6, 1.5 and 3.8 mm are available at the instrument.

Recently we were able to demonstrate at POLDI that the pulse-overlap method can also be used in transmission geometry, in a method referred to as Frame Overlap Bragg edge Imaging (FOBI) [24]. A standard high-resolution Micro-Channel Plate (MCP)/Timepix imaging detector [25] suitable for ToF imaging was utilized in the presented experiments. The detector has a pixel size of 55 μm and a field of view (FoV) of ~28 × 28 mm^2. A ToF spectrum is recorded in each pixel of the detector. The flight path, i.e. the distance from the chopper to the detector, was about 14 m. The maximum beam size at the measurement position is approximately 8 × 40 mm^2, smaller in width than the FoV of the detector. Based on the wavelength spectrum available at POLDI and the chopper parameters, the wavelength band effectively probed by the FOBI technique ranges from 0.96 Å to 3.28 Å [24].

2.3. Measurements

For specific crystal lattice planes, with lattice spacing d_{hkl}, neutrons with a wavelength λ are coherent-elastically scattered from the planes which are aligned at an angle θ to the incident beam according to Bragg's Law

$$\lambda = 2d_{hkl}\ sin\ \theta. \tag{1}$$

The diffraction angle rises with the wavelength until 2θ is equal to 180° or $\lambda = 2d_{hkl}$. Beyond this wavelength, the Bragg condition can no longer be satisfied for the specific set of hkl, resulting in a sharp increase in the transmitted intensity, the so-called Bragg edge. The Bragg edges in the transmission spectra are recorded in each pixel of an imaging detector.

The wavelength of the Bragg edge, hence, gives a direct measure of $2d_{hkl}$, while the height of a particular Bragg edge is, amongst others, related to the number of crystallites having their planes oriented perpendicular to the incident beam. Deviations of d_{hkl} from the nominal unstressed lattice spacing $d_{0_{hkl}}$, when the material is under stress, result in shifts of the diffraction angle for a given wavelength, but also a corresponding shift of the Bragg edge wavelength in transmission. Accordingly, when the strain-free spacing $d_{0_{hkl}}$ is known, strains ε can be retrieved according to the definition

$$\varepsilon_{hkl} = \frac{d_{hkl} - d_{0hkl}}{d_{0hkl}}. \tag{2}$$

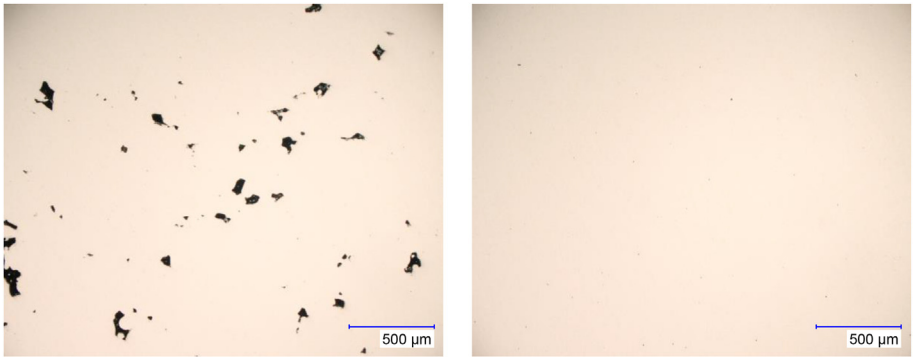

(a) Sample G (b) Sample A

Fig. 1 – Optical micrographs of the 316L and IN718 samples produced in different processing regimes, exemplarily showing (a) a sample with pronounced LoF porosity and (b) a dense sample.

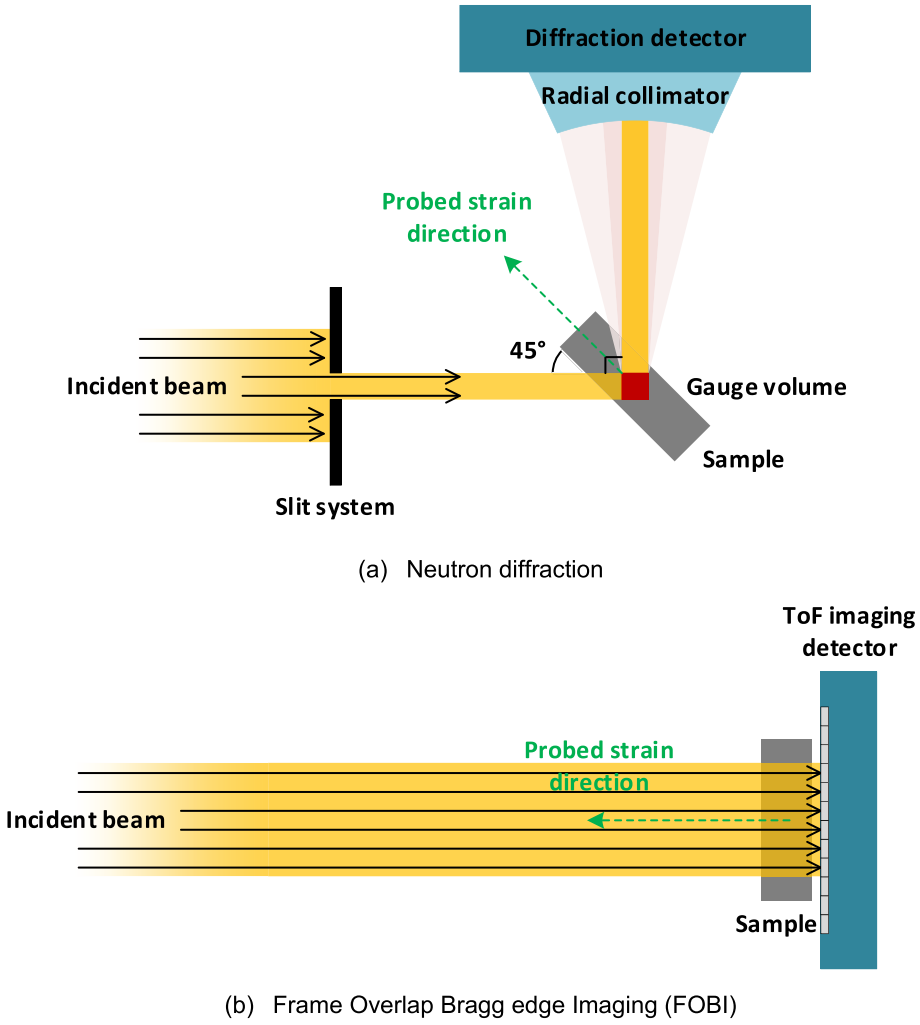

Fig. 2 – Schematics of the measurement setups at POLDI.

Ultimately, the stress components are computed using the plane-specific elastic constants (E_{hkl}, υ_{hkl}), the three normal strain components (ε_{11}, ε_{22}, ε_{33}) and the generalized Hooke's Law, for example

$$\sigma_{11} = \frac{E_{hkl}}{1+\upsilon_{hkl}} \cdot \left(\varepsilon_{11} + \frac{\upsilon_{hkl}}{1-2\upsilon_{hkl}} \cdot (\varepsilon_{11} + \varepsilon_{22} + \varepsilon_{33}) \right), \quad (3)$$

where E_{hkl} and υ_{hkl} are the plane-specific Young's modulus and Poisson's ratio, respectively.

2.3.1. *Neutron diffraction*

Neutron diffraction experiments were performed on the as-built 316L samples built in CM (A, B) which were still attached to the base plate. A total of 11 and 15 equally spaced measurement points, as schematically shown in Fig. 3, were selected for sample A and sample B, respectively. For each point, a gauge volume of 3.8 × 3.8 × 3.8 mm^3 was defined, which was fully submerged in the sample. All three principal strain components were probed for each point, i.e. along the transverse directions (TD1 and TD2) and the building direction (BD), utilizing a chopper speed of 5000 rpm. The exposure time for each measurement was chosen to be between 15 and 20 min as required to achieve adequate counting statistics. The raw data were reduced and fitted using the open-source software Mantid [26].

For strain evaluations, it is necessary to select the diffraction plane that is least affected by intergranular and inter-phase strains in order to properly determine the macroscopic residual stresses. Therefore, the 311 diffraction peak was utilized, which is recommended for that reason for face-centered cubic (FCC) Fe-based alloys [27–29] such as stainless steel 316L. In the present study, for the calculation of residual stresses the plane-specific elastic constants $E_{311} = 184\ GPa, \upsilon_{311} = 0.294$ were used for 316L taken from Ref. [30].

2.3.2. *Neutron Bragg edge imaging*

Bragg edge imaging (BEI) experiments were carried out on the as-built samples with a 30-mm building height (B, C, D, E, F, G). The schematic of the setup is shown in Fig. 2(b). The BEI data were acquired at a chopper speed of 2000 rpm. This configuration of chopper speed, flight path and chopper apertures implies a wavelength resolution range of 1.6%–0.47% for wavelengths from 0.96 Å to 3.28 Å. In order to acquire sufficient statistics for the significant spatial resolution, i.e. a large

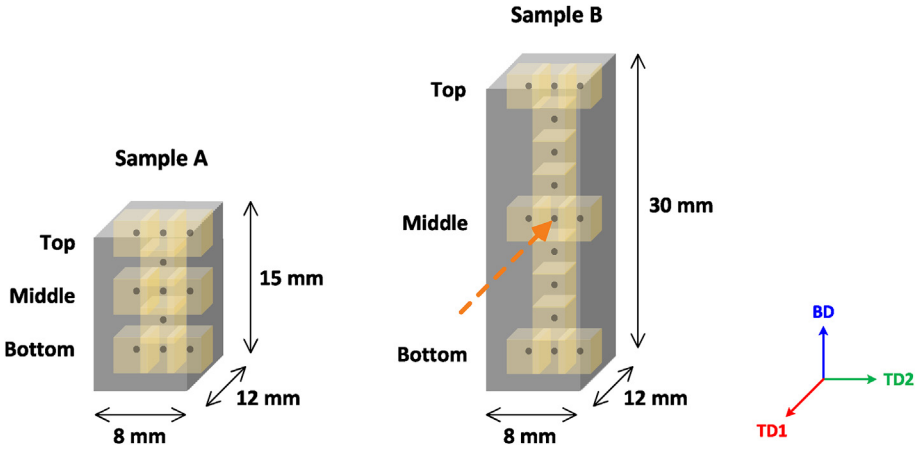

Fig. 3 – Schematic of the samples used in the neutron diffraction experiments showing the location of the measurement points, i.e. the gauge volumes. The coordinate axis corresponds to the strain/stress measurement coordinate system. The dashed orange arrow points to the beam direction in transmission.

number of pixels which corresponds to around 75,000 measurement points compared to 15 in diffraction, at a flux of 6×10^6 n/cm^2/s at POLDI, exposure times ranging from 16 to 20 h were used. A 5 × 5-pixel running average was performed to improve the counting statistics. The strain component probed was along TD1, i.e. the incoming beam being perpendicular to the 8 mm wide face and the height of the samples, as schematically shown in Fig. 3. The determination of a full stress tensor by BEI is not possible since the obtained strains are only along one specific direction. Additionally, for reference, the experiments were performed on a separate 316L and IN718 powder contained in a smaller Al tube with a lower exposure time of approximately 10 h.

2.4. *Strain-free reference*

The as-built 316L and IN718 samples produced in CM (A, B, E) were separated from the base plate by Electric Discharge Machining (EDM). Sample A was then annealed for 2 h at 650 °C. The treatment temperature was selected to achieve maximum stress relief with minimum change in microstructure, e.g. recrystallization, grain growth, grain coarsening and coalescence of inclusions and precipitation of other phases [31]. In contrast, after the separation from the base plate, a small rectangular cuboid of 5 × 5 × 30 mm^3 was cut out of the center of samples B and E and was sliced into a comb-type structure by EDM as depicted in Fig. 4 in order to relax the stress field. The comb-type cut was expected to relieve type I stresses (macrostresses), while type II (intergranular) and type III (atomic scale) stresses are retained by the cutting procedure [32].

The d_0 reference measurements with BEI were carried out on the comb-type samples B and E. For neutron diffraction, the reference measurement was performed in the middle of the annealed sample A with a gauge volume of 3.8 × 3.8 × 3.8 mm^3 as illustrated in Fig. 4.

2.5. *BEI lattice spacing evaluation methods*

In conventional ToF imaging, a ToF imaging detector is placed at a distance L from a pulsed neutron source. The detector counts for each pixel and time t the number of neutrons $N(t) = I(t)\Delta t$ arriving between times t and $t + \Delta t$ after the pulse generation time t_0. The number of neutrons transmitted by a specimen relative to the number of incident neutrons is wavelength dependent and can be expressed by the Beer-Lambert law as

$$T(\lambda) = \frac{I(\lambda)}{I_0(\lambda)} = e^{-\int \mu(\lambda) dl}, \tag{4}$$

where $I_0(\lambda)$ and $I(\lambda)$ are the incident and transmitted intensities, λ is the wavelength, l denotes the path through the sample and μ is the linear attenuation coefficient. The measured neutron flight time t, which varies due to the different velocities at different wavelengths, and the source-detector distance are used to directly transform the measured ToF t to the wavelength λ of neutrons arriving at the detector through

$$\lambda = \frac{ht}{mL}, \tag{5}$$

where h is the Planck constant and m is the neutron mass. The neutron wavelength λ_{hkl} of a Bragg edge for a specific plane (hkl) corresponds according to the Bragg equation with $\theta = 90$ to the lattice parameter $d_{hkl} = \lambda_{hkl}/2$. In FOBI measurements, however, multiple neutron pulses k with multiple possible pulse times t_0^k are superimposed at the detector. This superimposition hinders the direct determination of the time-of-flight t of a detected neutron. In this work, the approach of Ref. [24] to retrieve the transmission function in FOBI is adopted. The method allows the retrieval of the non-overlapping spectra $I(\lambda)$ and $I_0(\lambda)$ through Fourier deconvolution of the measured overlapped signal $I^K(\lambda)$ and $I_0^K(\lambda)$ utilizing the Wiener coefficient c in the equation

$$I(t) = \mathscr{F}^{-1}\left\{ \frac{\mathscr{F}\{I^K\}\,\mathscr{F}\{\Delta\}}{|\mathscr{F}\{\Delta\}|^2 + c} \right\}. \tag{6}$$

The Wiener coefficient was set to 0.1 for the data reduction and allows for direct deconvolution of the data when noise is considered in the convolution model. The incident beam

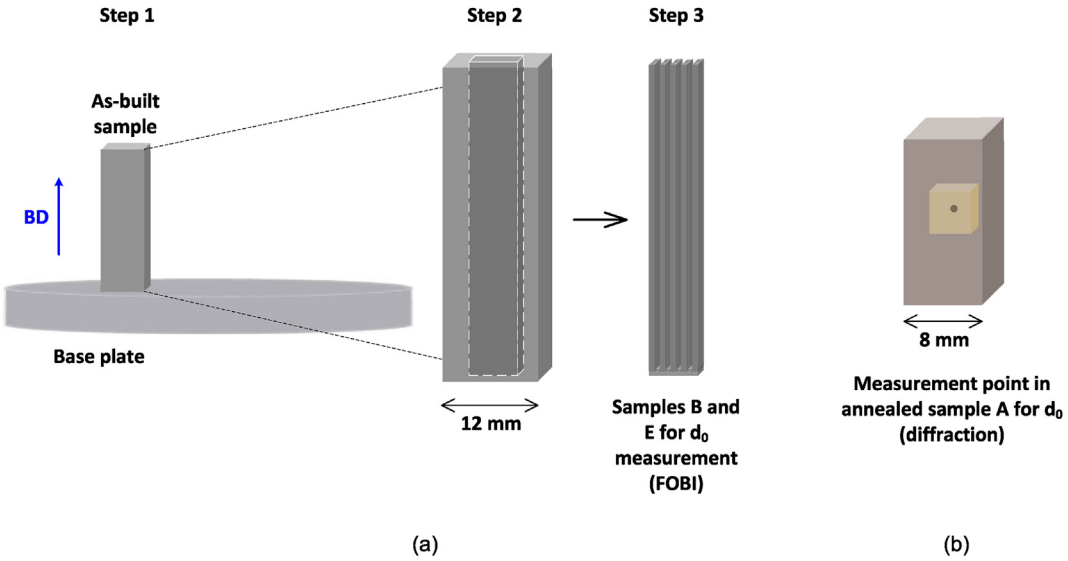

Fig. 4 – Schematic of the d_0 sample preparation: a) the sample is removed from the base plate (step 1), a 5 × 5 × 30 mm^3 piece is extracted by EDM (step 2) and comb-type sectioning is performed by EDM (step 3); b) the measurement point in the annealed sample A.

spectrum $I_0(t)$ can be obtained in the same way using Eq. (6). This FOBI data reduction approach returns the transmission as a function of time $T(t) = I(t)/I_0(t)$.

To obtain an accurate transformation from the measured arrival time t_m to wavelength λ, firstly the time offset t_0' between the trigger and the actual pulse time t_0 has to be known, which implies that the ToF $t = t_m - t_0'$. In addition, the flight path length L has to be known with sufficient accuracy [33]. The corresponding calibration was achieved by measuring the Bragg edge wavelengths of a body-centered cubic (BCC) iron powder standard with well-known lattice parameters and distinct Bragg edges. The considered lattice planes for the calibration were the (321), (220), (211) and (200) due to their strong Bragg edges profile as shown in Fig. 5(a). To allow the determination of L and t_0', the linear fit between the measured ToF values of the Bragg edges and the corresponding well-known Bragg edge wavelengths was performed. Since the chopper cuts through the beam horizontally, the Bragg edge wavelength of identical lattice planes varies slightly over the width of the beam, as shown in an example in Fig. 5(b) for the (200) lattice plane. Due to this, the calibration was performed in vertical slices of 5 × 512 pixels.

The transmission of a specimen as a function of neutron wavelength $T(\lambda)$ is directly related to the wavelength dependent microscopic total cross-section $\sigma_{tot}(\lambda)$ of the specimen as

$$\mu(\lambda) = N\sigma_{tot}(\lambda) \tag{7}$$

where N is the number density of the corresponding nuclei. The total cross-section is the sum of all elastic and inelastic, coherent and incoherent scattering contributions as well as the absorption that contributes to the beam attenuation. Bragg scattering is the coherent elastic contribution, which for some polycrystalline materials like steel and Ni alloys dominates the attenuation spectrum.

In this work, for each sample, two different phases can be considered to attenuate the beam, i.e. the powder and the additively manufactured specimen, while the Al tubes can be assumed sufficiently transparent for the neutron beam [34]. The final transmission $T(\lambda)$ is, therefore, the product of the transmission of both phases

$$T(\lambda) = T_s(\lambda)\, T_p(\lambda), \tag{8}$$

where s and p are designations for the additively manufactured *sample* and the *powder*, respectively. Since the goal is to extract the strains relative to the additively manufactured sample from the transmission spectrum $T_s(\lambda) = T(\lambda)/T_p(\lambda)$, $T_p(\lambda)$ is extracted based on separate measurements of the powder.

The powder and the dense additively manufactured sample differ significantly in their linear attenuation coefficients $\mu(\lambda)$, which is particularly due to the different atomic number densities. Even though the incident beam is attenuated by the same material, hence a very similar total cross section for a particular neutron wavelength, the number of atoms in a cubic centimeter of fine powder and dense bulk differs substantially. To obtain the linear attenuation coefficient of the powder $\mu_p(\lambda)$, Eq. (4) is rearranged and by using the measured powder transmission $T_p(\lambda)$ for a given neutron path length within the powder l_p

$$\mu_p(\lambda) = \frac{-\ln\left(T_p(\lambda)\right)}{l_p}. \tag{9}$$

The calculated linear attenuation coefficient of the powder can then be used to determine the powder transmission for any given l_p. In this case, l_p differs due to the difference in specimen size, i.e. the use of two different inner diameters of Al tubes which implies a varying amount of powder surrounding the additively manufactured sample with the same dimension. Moreover, the additively manufactured sample has a parallelepiped structure, while the powder is contained

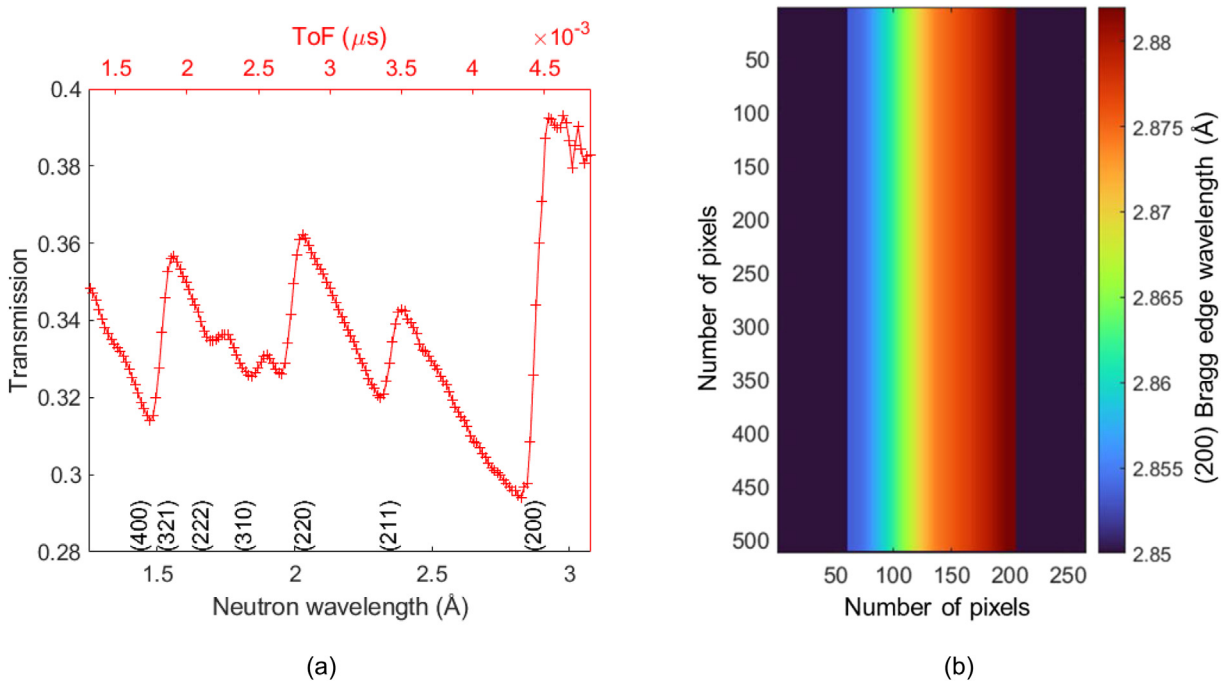

Fig. 5 – (a) The measured Bragg edge wavelengths of the BCC iron powder standard and (b) the Bragg edge wavelength λ_{200} plotted across the beam width.

in between the parallelepiped sample and the cylindrical Al tube. As a consequence, the value of l_p also varies across the field of view depending on the local geometry, i.e. beam path through the sample system.

The Bragg edge wavelengths were extracted by fitting a Gaussian to the first derivative of the extracted $T_s(\lambda)$ in a limited wavelength bandwidth containing the (311) Bragg edge at about 2.2 Å. The fitted Bragg edge wavelengths λ_{311} of both as-built and strain-free reference samples yield residual strain maps according to Eq. (2).

3. Results and discussion

3.1. *Measured strain-free reference values*

Annealing at high temperatures can adequately remove residual stresses in 316L, but as a consequence, it considerably changes the microstructure from the as-built state. In contrast, d_0 measurements on 316L samples annealed below their solutionizing temperatures do not have a significant influence on the microstructure but were known to incompletely relieve residual stresses to a certain degree [31]. For the d_0 determination, the middle part of sample A was measured with neutron diffraction along TD2, which resulted in a d_0 of 1.08418 Å. The d_0 was remeasured with BEI to calculate the residual strains in as-built samples B, C and D using the combcut sample B. In this case, no significant trend with distance from the top surface in d_0 of sample B is seen and thus an average value was used.

In the case of IN718 samples, annealing was avoided as the resulting changes in lattice spacings of Ni-based superalloys might not be merely caused by lattice relaxations, but they can also be influenced by phase transformations or precipitations of several different phases, which change the chemical composition of the matrix and hence the lattice spacing [35]. In addition, the accumulated thermal gradient throughout the layer-by-layer manufacturing process in Ni-based superalloys might introduce heterogeneity in microstructure and thus chemical composition along the sample height. Thus, the linear fit of d_0 values from BEI that tend to increase towards the top surface of sample E, as shown in Fig. 6, was used for residual strain calculations in as-built samples E, F and G to take into account the aforementioned possible slight variations.

3.2. *Neutron diffraction results*

Fig. 7 shows the residual stress values for samples A and B in the as-built condition. The error bars indicate the error propagation in peak determination through peak fitting. Since samples A and B were built with the same parameters, the evolution of residual stresses over the height in all orthogonal directions of both samples follows a similar tendency with nearly the same values. It can be seen in Fig. 7(b) that the residual stresses reach a plateau after about 11 mm below the top surface, while the stresses increase monotonically up to about 11 mm from the top surface, which is in agreement with Mercelis et al. [36] who measured residual stresses in samples with heights only up to 10 mm.

The relatively high compressive stresses along BD that decay towards the top surface (Fig. 7) correspond to the Temperature Gradient Mechanism (TGM) [36–39], which very well explains the formation mechanism of residual stresses in laser-treated materials in the building direction. The heat introduced to the material causes the heated zone to expand,

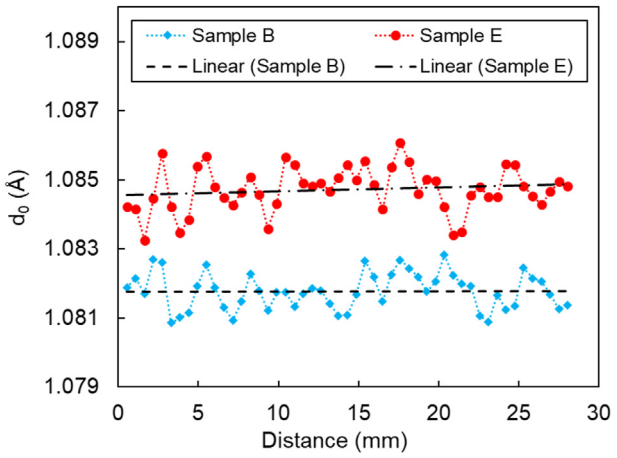

Fig. 6 – d_0 measurement results of samples B and E obtained from BEI. The x-axis indicates the distance from the topmost surface of the sample.

but the expansion is constrained by the surrounding solid, inducing compressive or more negative stresses around the heated zone. If the stresses surpass the yield strength of the material, they become partially elastic and partially plastic. The heated zone then shrinks as it cools down, but the shrinkage is restricted by the previously formed plastic deformation, introducing tensile or more positive stresses in the added top layer.

In the transverse directions, the mechanism of the residual stress development is the constrained contraction mechanism, which implies that the most significant residual stresses are created parallel to the scanning vectors [39]. The constrained contraction of material upon cooling occurs as a result of the steep thermal gradients following solidification. Due to this, there is a mismatch in the degree of shrinkage which becomes prominent as tensile stresses in the upper region of the part. This mechanism can be, however, suppressed by the bidirectional scanning strategy with an alternating rotation of 67° used in this work. The state of stresses σ_{TD1} alternates from slightly tensile close to the base plate to slightly compressive along the middle region and back to a more significant tensile stress state closer to the top. A moderate tensile stress state with a similar profile as that of σ_{TD1} was observed in σ_{TD2} with a few measurement points showing relatively constant values close to 0 in both samples. The result agrees with the work done by Kruth et al. [37] who used the bridge curvature method and reported a substantial reduction in curling angles of the bridge, which depend on the residual tensile stresses measured in the plane of laser scanning.

3.3. *BEI results*

Fig. 8 and Fig. 9 show the map of residual strains along TD1 in samples printed with parameters to induce lack of fusion pores (C, D, F and G) and optimized parameters to achieve high density (B and E). As mentioned before, since the beam traveled across the sample and the corresponding powder, the transmission spectra recorded were the product of both phases. The use of different Al tube diameters was intended to verify the effectiveness of the disentanglement steps described in Section 2.5. By applying the steps, as shown in Fig. 8(b) and (c) for 316L and Fig. 9(b) and (c) for IN718, the disentanglement steps successfully removed the transmission spectrum of the overlying powders, regardless of the thickness, revealing nearly identical strain maps of the same material from the same processing parameters, i.e. samples C and D for 316L and samples F and G for IN718.

In Fig. 8(a) and Fig. 9(a), significantly higher tensile residual strains close to the free surfaces of the dense samples are observed. Neutron diffraction on sample B provides corresponding results, however, the phenomenon appears less prominent due to the limited spatial resolution of diffraction. Comparing these with the samples of the same material but featuring LoF porosity C, D, F and G, one finds that the tensile strains at the surface are less pronounced in these samples. This finding is possibly related to the influence of LoF porosity on the residual strains as the presence of porosity reduces the

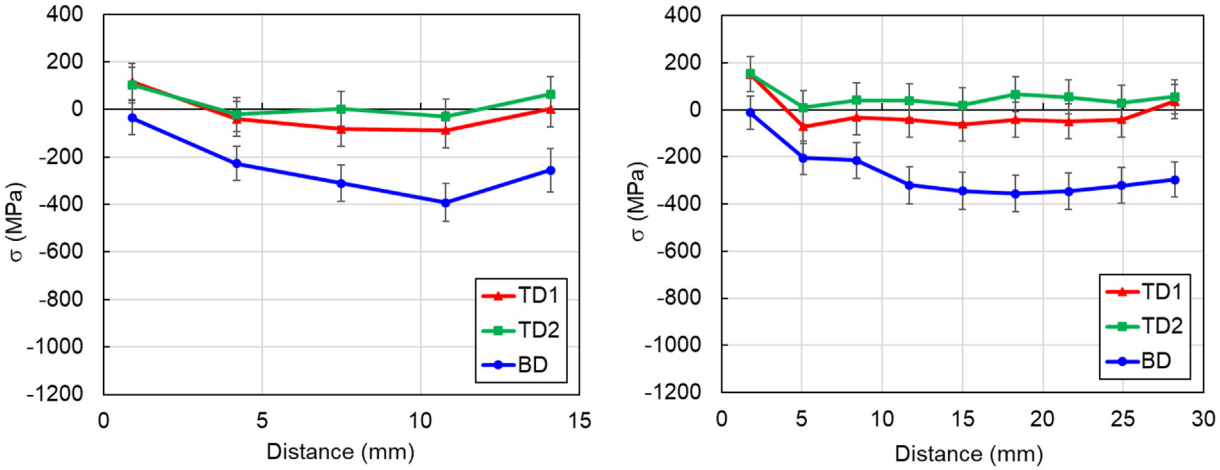

Fig. 7 – Neutron diffraction results showing residual stresses in 316L samples built in the conduction mode regime. The x-axis indicates the distance from the topmost surface of the sample.

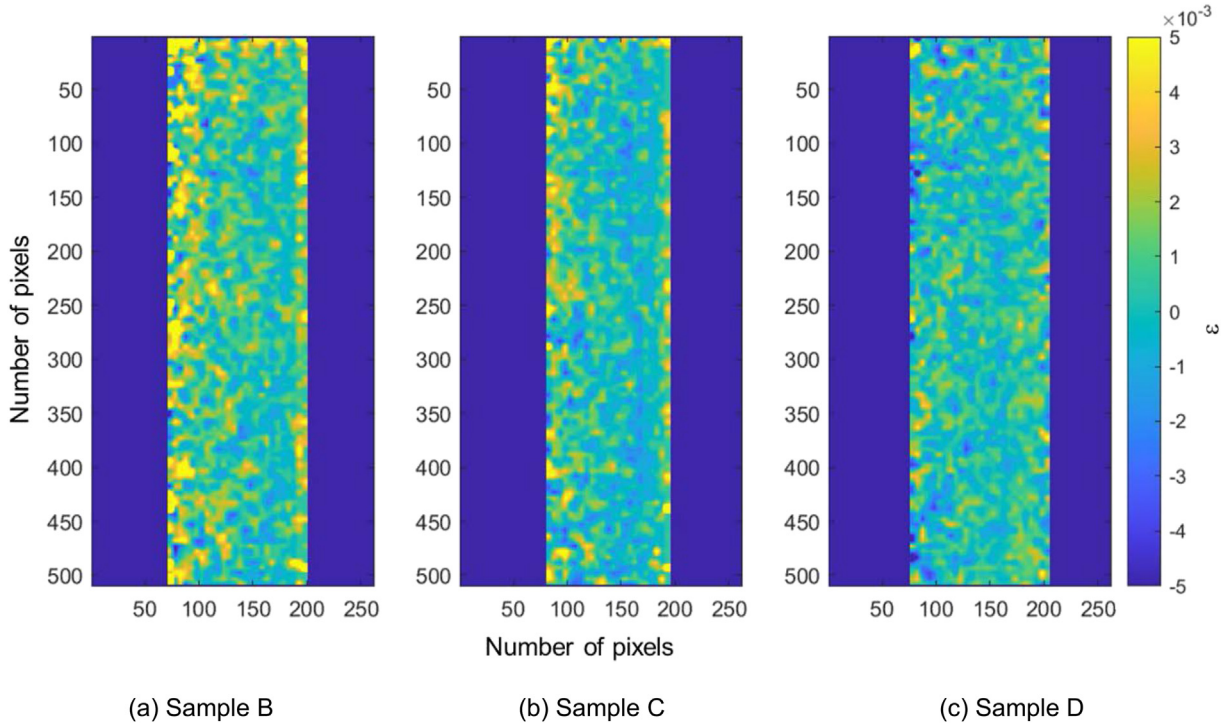

Fig. 8 – Residual strain maps of 316L samples measured along the TD1. The build direction is from the bottom to the top of the figures.

material constraints and, hence, the strains. The strain profiles plotted across the width at half the height of the samples in Fig. 10 also show that the strains in the IN718 samples are generally compressive whereas those in 316L tend to be tensile. BEI is very efficient in revealing the existence of steep strain gradients where tensile stresses exist at the outer surface of the samples, which agrees well with previous investigations [2,18].

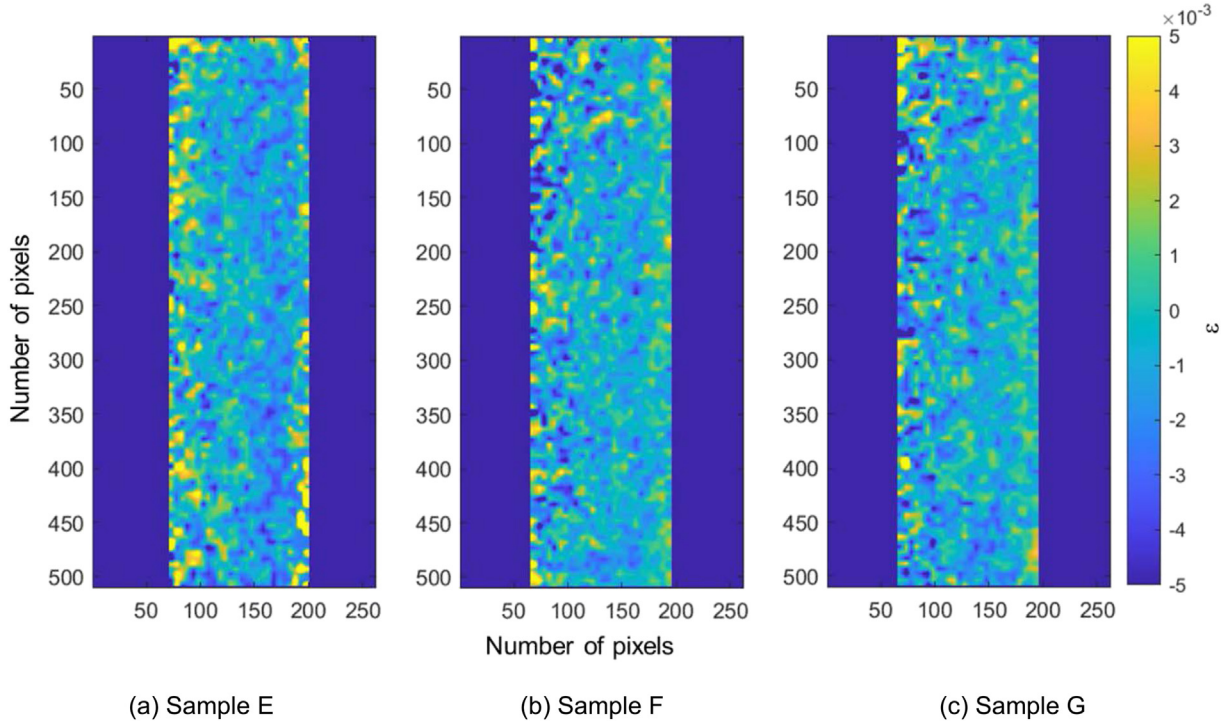

Fig. 9 – Residual strain maps of IN718 samples measured along the TD1. The build direction is from the bottom to the top of the figures.

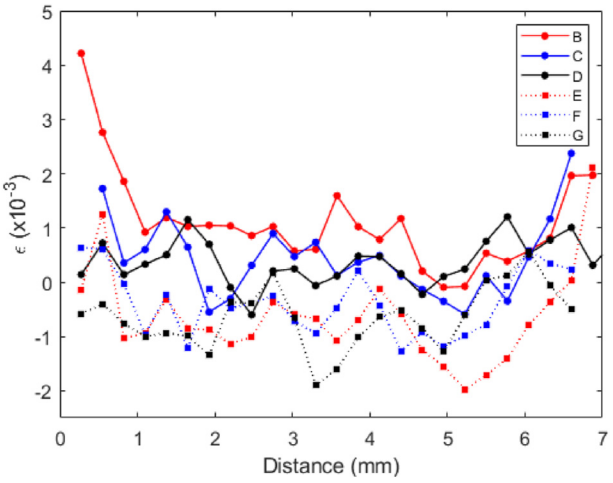

Fig. 10 – Strain profiles along TD1 across the width of the samples comparing 316L samples (solid lines) and IN718 samples (dotted lines). The colors indicate the same combination of processing regime and projected powder thickness distribution.

3.4. *BEI compared with neutron diffraction*

For a straight comparison of the results from BEI and neutron diffraction, the strain profiles of 316L samples along TD1 obtained from both methods are plotted in Fig. 11. The strains obtained with BEI were averaged over 69 pixels in width, which corresponds to one of the dimensions of the gauge volume in neutron diffraction, i.e. 3.8 mm. Along the building height, an averaging of only 10 pixels was performed to highlight the benefit of the spatial resolution from BEI. It can be seen in Fig. 11 that the residual strains in sample B measured using both methods are in good agreement, which implies that the disentanglement steps developed in this study work accurately.

The plotted strain profiles from BEI also exhibit a slightly higher magnitude of strains in the dense sample compared to the samples containing considerable porosity in particular with regards to the steep increase of the curves towards the top surface. The averaging effect of neutron diffraction is greatly evident in Fig. 11, as it fails to precisely reveal the steep strain gradient at the top part of sample B. This steep gradient close to the top surface, however, appears to be lower in the LoF samples (C, D) compared to the dense sample (B), as also shown in the strain maps (Fig. 8).

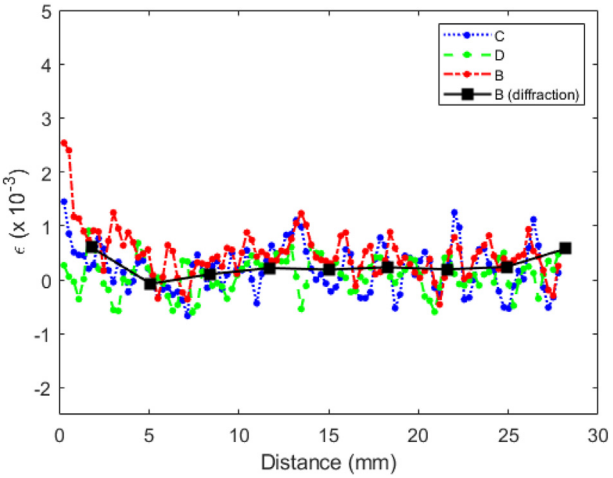

Fig. 11 – Strain profiles along TD1 obtained from BEI (dashed lines) and neutron diffraction (solid line). The x-axis indicates the distance from the topmost surface of the sample.

4. Conclusion

The residual strains in PBF-LB/M-built 316L and IN718 samples measured with BEI and diffraction were analyzed. The disentanglement steps to separate different contributions in the recorded spectra in BEI being a product of the transmission spectra from two different material states are presented. The extraction of the transmission spectrum of a PBF-LB/M printed sample embedded in its corresponding powder mimicking the circumstances in additive manufacturing was successfully performed. The results could be verified by utilizing different powder containers resulting in differently sized powder volumes around the corresponding samples which led to well-matching strain maps. The results of 316L samples from BEI were further verified through comparison with those obtained from conventional neutron diffraction, which agree very well with the BEI results.

BEI was found to capture better than neutron diffraction the strong gradients close to the top part of the samples due to its superior spatial resolution. The strain maps from BEI reveal the heterogeneity of the residual strains between the outer surface and the bulk of the samples. Tensile strains exist close to the free surfaces of the dense samples. The gradient was not captured by neutron diffraction as a result of the limited spatial resolution. The samples featuring LoF porosity demonstrated lower residual strains that are assumed to be caused by the presence of pores reducing the material constraints and therefore the resulting strains. The strain disentanglement from BEI, when measurements are undertaken through two different materials or material states, is particularly useful for operando and non-destructive strain characterization with neutrons during powder bed additive manufacturing or of additively manufactured multi-materials.

Declaration of Competing Interest

The authors declare that they have no known competing financial interests or personal relationships that could have appeared to influence the work reported in this paper.

Acknowledgments

This research was funded by the Swiss National Science Foundation (SNSF) under grant agreement No. CRSII5_193799. The project was enabled partially through funding from the Strategic Focus Area Advanced Manufacturing (SFA-AM), an initiative of the ETH Board and DanScatt. CN, RE and RL thank PX Group for the generous support to the LMTM laboratory.

REFERENCES

[1] Woracek R, et al. Diffraction in neutron imaging—a review. Nucl Instrum Methods Phys Res A 2018;878:18.
[2] Busi M, et al. Nondestructive characterization of laser powder bed fusion parts with neutron Bragg edge imaging. Addit Manuf 2021;39:9.
[3] Strobl M, et al. Time-of-flight neutron imaging for spatially resolved strain investigations based on Bragg edge transmission at a reactor source. Nucl Instrum Methods Phys Res 2012:8.
[4] Tremsin AS, et al. High-resolution strain mapping through time-of-flight neutron transmission diffraction with a microchannel plate neutron counting detector. Strain 2012;48:296–305.
[5] Woracek R, et al. Neutron Bragg-edge-imaging for strain mapping under in situ tensile loading. J Appl Phys 2011;109:4.
[6] Malamud F, et al. Texture analysis with a time-of-flight neutron strain scanner. J Appl Crystallogr 2014;47(4):1337–54.
[7] Santisteban JR, Edwards L, Stelmukh V. Characterization of textured materials by TOF transmission. Phys B Condens Matter 2006;385–386:636–8.
[8] Polatidis E, et al. Neutron diffraction and diffraction contrast imaging for mapping the TRIP effect under load path change. Materials 2020;13(6):1450.
[9] Steuwer A, et al. Using pulsed neutron transmission for crystalline phase imaging and analysis. J Appl Phys 2005;97.
[10] Woracek R, et al. 3D mapping of crystallographic phase distribution using energy-selective neutron tomography. Adv Mater 2014;26(24):4069–73.
[11] Woracek R, et al. Neutron Bragg edge tomography for phase mapping. Phys Procedia 2015;69:10.
[12] Iwase K, et al. In situ lattice strain mapping during tensile loading using the neutron transmission and diffraction methods. J Appl Crystallogr 2012;45.
[13] Hendriks J, et al. Bragg-edge elastic strain tomography for in situ systems from energy-resolved neutron transmission imaging. Physical Review Materials 2017;1.
[14] Hendriks JN, et al. Tomographic reconstruction of triaxial strain fields from Bragg-edge neutron imaging. Physical Review Materials 2019;3(11):113803.
[15] Wensrich CM, et al. Bragg-edge neutron transmission strain tomography for in situ loadings. Nucl Instrum Methods Phys Res Sect B Beam Interact Mater Atoms 2016;383:52–8.
[16] Busi M, et al. Bragg edge tomography characterization of additively manufactured 316L steel. Physical Review Materials 2022;6(5):053602.
[17] Makowska M, et al. Coupling between creep and redox behavior in nickel - yttria stabilized zirconia observed in-situ by monochromatic neutron imaging. J Power Sources 2017;340:167–75.
[18] Morgano M, et al. Investigation of the effect of laser shock peening in additively manufactured samples through Bragg edge neutron imaging. Addit Manuf 2020;34:101201.
[19] Tremsin A, et al. Investigation of dissimilar metal welds by energy-resolved neutron imaging. J Appl Crystallogr 2016;49.
[20] Tremsin AS, et al. Investigation of microstructure in additive manufactured Inconel 625 by spatially resolved neutron transmission spectroscopy. Sci Technol Adv Mater 2016;17(1):324–36.
[21] Tremsin AS, et al. Monitoring residual strain relaxation and preferred grain orientation of additively manufactured Inconel 625 by in-situ neutron imaging. Addit Manuf 2021;46:102130.
[22] Marattukalam JJ, et al. The effect of laser scanning strategies on texture, mechanical properties, and site-specific grain orientation in selective laser melted 316L SS. Mater Des 2020;193:11.
[23] Stuhr U, et al. Time-of-flight diffraction with multiple frame overlap Part II: the strain scanner POLDI at PSI. Nucl Instrum Methods Phys Res 2005;545:9.
[24] Busi M, et al. Frame overlap Bragg edge imaging. Sci Rep 2020;10(1):10.
[25] Tremsin AS, et al. High resolution Bragg edge transmission spectroscopy at pulsed neutron sources: proof of principle experiments with a neutron counting MCP detector. Nucl Instrum Methods Phys Res Sect A Accel Spectrom Detect Assoc Equip 2011;633:S235–8.
[26] Arnold O, et al. Mantid—data analysis and visualization package for neutron scattering and μ SR experiments. Nucl Instrum Methods Phys Res Sect A Accel Spectrom Detect Assoc Equip 2014;764:156–66.
[27] Hutchings MT, et al. Introduction to the characterization of residual stress by neutron diffraction. CRC press; 2005.
[28] ISO. ISO/TS 21432: Non-destructive testing—standard test method for determining residual stresses by neutron diffraction. Geneva: ISO; 2005.
[29] Webster GA, Wimpory RC. Non-destructive measurement of residual stress by neutron diffraction. J Mater Process Technol 2001;117(3):395–9.
[30] Rangaswamy P, et al. Residual stresses in LENS (R) components using neutron diffraction and contour method. Mater Sci Eng 2005;399:72–83.
[31] Chao Q, et al. The effect of post-processing heat treatment on the microstructure, residual stress and mechanical properties of selective laser melted 316L stainless steel. Mater Sci Eng 2021:821.
[32] Withers PJ, et al. Methods for obtaining the strain-free lattice parameter when using diffraction to determine residual stress. J Appl Crystallogr 2007;40:14.
[33] Tremsin AS, et al. Calibration and optimization of Bragg edge analysis in energy-resolved neutron imaging experiments. Nucl Instrum Methods Phys Res Sect A Accel Spectrom Detect Assoc Equip 2021;1009:165493.
[34] Vontobel P, Lehmann E, Frei G. Performance characteristics of the tomography setup at the PSI NEUTRA thermal neutron radiography facility. Proceedings of Computed Tomography and Image Processing for Industrial Radiology 2003:23–5.
[35] Gruber K, et al. Impact of high temperature stress relieving on final properties of Inconel 718 processed by laser powder bed fusion. Mater Sci Eng, A 2021;813:15.
[36] Mercelis P, Kruth JP. Residual stresses in selective laser sintering and selective laser melting. Rapid Prototyp J 2006;12(5):254–65.
[37] Kruth J-P, et al. *Assessing influencing factors of residual stresses in SLM using a novel analysis method*. 16th International Symposium on Electromachining. ISEM 2010:531–7. 2010.
[38] Kruth JP, et al. Assessing and comparing influencing factors of residual stresses in selective laser melting using a novel analysis method. Proc IME B J Eng Manufact 2012;226(6):12.
[39] Robinson JH, et al. The effect of hatch angle rotation on parts manufactured using selective laser melting. Rapid Prototyp J 2019;25/2:10.